Iridium substitution in nickel cobaltite renders high mass specific OER activity and durability in acidic media

Waqas Qamar Zaman[a], Wei Sun[a], Muhammad Tariq[a], Zhenhua Zhou[a], Usman Farooq[a], Zain Abbas[a], Limei Cao[a], Ji Yang[a,b,*]

[a] State Environmental Protection Key Laboratory of Environmental Risk Assessment and Control on Chemical Processes, School of Resources and Environmental Engineering East China University of Science and Technology, 130 Meilong Road, Shanghai, 200237, PR China
[b] Shanghai Institute of Pollution Control and Ecological Security, Shanghai, 200092, PR China

A B S T R A C T

Oxygen evolution reactions being kinetically sluggish and highly expensive remains bottleneck in high pressure hydrogen production from acidic solution water electrolysis. Process economization is mostly affected due to larger consumption of precious iridium as an anodic catalyst. Therefore, effective utilization of noble metal remains a major challenge to be overwhelmed. Comprehensive theoretical and experimental studies show electronic dependency on different structural motifs of IrOx. However, due to lack of suitable non-noble host structures for iridium substitution there is hindrance in implementation. In current study, we explored inverse spinel, nickel cobaltite, as a host structure that provides OER beneficial structural motif to iridium sites on account of relatively higher IrO_6 edge sharing than in rutile IrO_2. Compact presence of octahedras in host structure reduces Ir–Ir bond length for neighboring IrO_6 octahedral units in it that further intrinsically improves the iridium sites due to electronic modulations. Specifically, composite comprising 20 mol% iridium in $NiCo_{2-x}O_4$ rendered acid stable 15 folds enhancement in mass specific OER activity relative to IrO_2 resulting in substantial reduction of iridium content. Fabricated composite displayed an onset potential and tafel slope of 1.425 V and 40.4 mV dec^{-1}, respectively in relative to 1.475 V and 68.1 mV dec^{-1} for pure IrO_2. Current approach for effectively utilizing precious metal will lead in future for economizing hydrogen production via water splitting.

1. Introduction

Escalation in energy consumption throughout the globe have driven intense exploration for alternate energy resources and its storage. Electrochemical production of hydrogen via water electrolyzers [1], rechargeable batteries [2], unitized fuel cells [3] and redox flow batteries [4] is contemplated to play a decisive role in the current quest of energy conversion and its bulk storage. Acidic environment water electrolysis through polymer electrolytic membrane is emerging as a promising technique for pure carbon free production of hydrogen at high pressures (over 150 bar) without significant requirement of additional compression. Moreover, low pH water electrolysis is also well-known to ease H_2 generation over platinum based cathode materials [5,6]. However, large scale application of this technology is momentously hindered due to sluggish kinetics of coupled oxygen evolution reaction (OER) at anode and its stability towards harsh acidic

media. Significantly higher energy requirements, as overpotential at anode to achieve moderate current densities, elevates the production cost as compared to other technologies [7] and strictness in the usage of iridium and its oxides. Therefore IrO_2, being expensive and only known robust catalyst in acidic environment, will definitely impede global adoption of PEM fuel cells to counter energy crisis. Thus, to support the execution of hydrogen-based power supplies cost effectiveness of PEM electrolyzers, in terms of effective utilization of iridium, remains a major challenge to be overwhelmed.

Since quicker and stable OER kinetics in acidic media mainly centers around iridium therefore various approaches are being applied to maximize the effective utilization of precious metal [8–13]. All such methods are either classified as engineered approaches or as ones intrinsically modifying the metallic species, where the later serves as a fundamental to the former for the rational designing of the efficient catalysts. While, very few approaches have been reported showing

successful implementation of intrinsically improved iridium sites against acid corrosive environment, at its minimal consumption [14,15]. Recently reported higher ratio of corner to edge sharing IrO_6 octahedra has been termed as structural descriptor for higher OER activity due to intrinsically improved iridium centers [16]. Actually, shortened Ir−Ir bond length of neighboring iridium centers for such structures lead to more electronic occupation of Ir-5d states that eventually improves the OER catalytic activity [17]. Even though enhancement in activity is achieved but still high fraction of precious metal in these composites remain undealt. In this regard, considering a host structure that possesses higher ratio of corner to edge sharing octahedra and permits iridium substitution into its lattice system would serve as an effective economizing approach.

In quest of such structure we identify nickel cobaltite, inverse spinel, as a suitable candidate for the aforementioned task. As each octahedral unit in it has six edge shared octahedras and six corner shared tetrahedras that gives OER structural descriptor ratio of 1 being relatively more than rutile IrO_2 possessing 0.25. Secondly, nickel cobaltite as a host structure allows incorporation possibility of almost over 30 different ions lying in radii range of 0.5–1.0 Å [18]. These structural features prompted us to study the possible OER beneficial intrinsic improvement of iridium upon occupation in this structure. Accordingly, we report here successful formation of ternary iridium nickel cobaltite composites exhibiting robust electrochemical activity and stability. Specifically, iridium in spinel having an overall 0.2 M fraction of content was found extremely durable and exhibited almost over 15 folds mass specific enhancement in OER activity than state of the art catalyst IrO_2. The applied characterization techniques of x-ray diffractometry analysis (XRD), transmission electron microscopy (TEM), x-ray photoelectron spectroscopy (XPS) and x-ray adsorption spectroscopy (XAS) verified structural dependent electronic modulations of iridium sites that rendered momentous intrinsic improvement to precious metal. Therefore, our engineered approach unveils a ternary iridium nickel cobaltite composite that at minimal iridium's consumption behaves as a robust electro catalyst toward acid corrosive environment. Results achieved from the current study would surely prove in opening of more such avenues towards economical and rational designing of anodic catalyst for efficient water splitting.

2. Experimental section

2.1. Composite synthesis $Ir_xNiCo_{2-x}O_\delta$

Iridium nickel cobaltite composites with varying concentrations were hydrothermally synthesized followed by a post annealing treatment to enhance effective product crystallinity. Iridium (III) chloride hydrate ($IrCl_3 \cdot 3H_2O$) and hydrated nitrate salts of Nickel and Cobalt i.e., $Ni(NO_3)_2 \cdot 6H_2O$ and $Co(NO_3)_2 \cdot 6H_2O$ were taken as precursors for the metal constituents. As, per required molar concentration the calculated volume of salt solutions were taken in 50 ml Teflon bottles followed by the addition of 0.4 mL H_2O_2 as an oxidizing agent in it. Next, before the addition of 15 ml 0.5 M NaOH, residence time of half an hour was given for added oxidizing agent's interaction with metallic salt solutions. Later, the bottles after being placed in autoclaves were kept in an oven at 200 °C for heat treatment of 10 h. Hydrothermally obtained product was then washed thrice, to ensure removal of unwanted species, with deionized water and was suction filtered to get synthesized composite as retentate. Filtrated product after the drying process at 60 °C for half an hour was carried for an annealing treatment in furnace for 10 h at 400 °C.

2.2. Electrode preparatory method and electrochemical measurement

The employed electrodes, dimensionally stable anode type (DSA), in current study were prepared by pasting 7.5 μL of a homogeneous electrode ink on 0.5 cm × 1.5 cm Ti plate. Ink deposition step was repeated five times to obtain catalyst loading amount of around 0.2 mg cm^{-2}. Whereas, the electrode ink was prepared by dispersing 6 mg of catalyst powder in 1.5 mL of 2:1 v/v isopropanol/water, followed by sonication for 1 h. The Ti plates used here were prior etched by 10% (wt %) oxalic acid for 2 h near boiling conditions followed by rinsing with deionized water. A three electrode cell was employed for all electrochemical measurements of prepared electrodes. Dimensionally 0.5 cm × 0.7 cm (electrode reactive area = 0.35 cm^2) of the prepared DSA served as working electrode, as the remaining was insulated, except for a small part for connecting the wire. A cleaned Pt foil with a 1 cm × 1 cm exposed area was used as counter electrode along with a saturated calomel reference electrode (SCE). Electrolyte used for the process was 0.1 M $HClO_4$ solution, and deionized water was used as solvent, where all other chemicals employed were of analytical grade. The obtained electrode potentials were converted to reversible hydrogen electrode (RHE) from SCE scale by calibrating with (NHE) = E (SCE) + Ej = 0. The over potential values were obtained using equation η = $E_{Applied}$ (RHE) − iR − 1.229 after being corrected with uncompensated ohmic electrolyte resistance measured via electrochemical workstation (CH Instruments Ins., CHI660E) at the open circuit 10 mV potential in 0.1 M $HClO_4$ solution. The data from polarization curves was recorded after being cycled at least five times or until the overlapping of curves was observed. Stair-case voltammetry method was employed for conductance of Tafel plots at different potential range under the scan rate of 0.1 mV s^{-1}.

2.3. Physical characterization techniques

Surface area of the prepared composites was obtained using Micromeritics Tristar 3020 by BET method. The crystallographic investigation of catalyst was accomplished using powder X-Ray diffraction (XRD) using a D/max2550 V apparatus with a Cu-Kα radiation source (λ = 1.5406 Å), at a step size of 0.02° over a range of 10°–80°. Field-emission scanning electron microscope (FESEM) equipped with a Nova NanoS and the Energy dispersive X-ray (EDX) spectrometer were employed for observance of morphology and compositional analysis using TEAMApollo system respectively. The TEM and HRTEM images were obtained using JEM-2100 transmission electron microscope. X-ray photoelectron spectroscopy (XPS) analysis of the prepared catalyst was obtained using an ESCALAB 250Xi instrument with an Al-Kα radiation source at an energy step size of 0.05 eV for high resolution XPS spectrum aided in determination of surface properties. The spectra obtained from XPS analysis was calibrated with respect to C-$1s$ at a binding energy of 284.6 eV, as samples were sputter coated with carbon. The X-ray absorption data (XAS) at the Ir L_{III} edge of samples, after being mixed with LiF to reach 50 mg, were recorded in transmission mode at room temperature within ion chambers using the $BL_{14}W_1$ beam line of Shanghai Synchrotron Radiation Facility (SSRF), China, operated with a Si (111) double crystal mono-chromator. During measurements, the synchrotron was operated at an energy of 3.5 GeV and a current between 150–210 mA.

3. Results and discussion

Nickel cobaltite, a promising candidate of cobaltite family, possesses an inverse spinel structure whereas iridium in its oxide form exists in rutile structure. As, there is a considerable difference in the crystal system of oxides so the lattice mismatch would restrict noble metal insertion to a certain level in spinel structure. The former is composed of tetrahedral and octahedral sites, where nickel ions are present at octahedral sites and cobalt ions reside equally distributed in both octahedral and tetrahedral sites [19]. In order to substitute iridium in spinel structure, certain different amounts (6%, 12%, 20% and 25%) of noble metal were selected to substitute the cobalt at octahedral sites. As Shi et al. confirms octahedral sites of Co being relatively more favorable for generation of vacancies due to lower formation energy than

the counterpart [20]. The fabricated composites upon iridium doping were named as x-IS, where x (6, 12, 20 and 25) represents the molar percentage of dopant and IS denotes iridium in spinel ($NiCo_2O_4$).

3.1. Structural characterization using XRD, TEM and Ir-L_{III} EXAFS

X-ray diffractogram analysis gives valuable indication for the doped structures possessing a lattice mismatch between the species in terms of diffraction angle shift. According, to Hume Rothery substitution rule a difference of ≤15% between the ionic radii of solute and solvent can undergo the desired substitution within a crystal lattice. This difference extent due to lattice mismatch between the species along with the doped amount corresponds to the occurrence and extent of shift in diffraction angle. The performed X-ray diffractogram analysis for all prepared mixed composites in the current study, irrespective to phase restriction, elucidated presence of iridium in terms of decreased diffraction angle. Diffraction patterns obtained for both prepared pure iridium dioxide and nickel cobaltite were well in consistent to pdf chart # 15-0870 and 20-0781, respectively. Whereas, for all mixed composites a shift was observed, with respect to iridium concentration, towards lower angle from the diffraction pattern of nickel cobaltite. Such reduction in plane's angle is always attributed to the arising variations in cell parameter due to the substitution of specie with relatively different radius as shown in Fig. 1a [21]. Fig. 1b presents the inset of Fig. 1a with selected angle range clearly showing the gradual declination of diffraction angle for increasing iridium content. Subsequently, it indicates a change of unit crystal structure with increasing iridium content that infers substitution of larger size iridium [22]. Moreover, a decrease and increase in values of main peak (311) diffraction intensity and full width at half maximum (FWHM) were observed, respectively, further implying successful substitution of iridium that decreases the crystallinity of doped composites as obvious from Fig. 2 [23,24]. Among, all the iridium containing samples an arousal of shoulder peak was observed in case of 25-IS, containing 25 mol% iridium content, at

an angle of 35.3°. The diffraction footmarks of this aroused peak were difficult to relate exactly any of the possible oxide formation in the current study. The closest plane (101) of IrO_2 was found to be present at further lower angle to this emergent peak, which elucidates later on favorable formation of rutile structure for higher contents of iridium and a limit to iridium inclusion below this by host structure. Therefore, this peak could be attributed to the rutile existence of iridium dioxide doped by both nickel and cobalt [13]. Hence, it could be deduced that iridium incorporation in nickel cobaltite could be possible till approximately 20% mol fraction.

The observed structural modifications of spinel structure were also well depicted from transmission electron microscopic images and scanning electron microscopic images shown in Figs. 2 and S3. It was observed that iridium inclusion in spinel had increased the d-spacing due to its larger radius resulting in formation of deteriorated crystals for doped composite. Moreover, a gradual decrease in BET surface area of doped composites was obtained with respect to increasing iridium concentration as presented in SI. The change in surface area value is often reported for the doped samples compared to pure metal oxides, which may result due to change in particle size, agglomeration or due to the limitation of single state adsorption model of BET for the surface present inhomogeneity. In present study along with the latter, agglomeration in doped samples was observed as seen from Fig. S5, which can be attributed to the lowering of surface area. The obtained results are consistent to earlier conducted study for manganese substitution in $NiCo_2O_4$ [25]. In order, to explore further the induced geometric changes in crystal system by the noble metal, we acquired X ray absorption spectroscopic analysis (XAS) of iridium in all the mixed composites and in IrO_2. Results obtained from Fourier transforms of k_3-normalized Ir-L_{III} edge x-ray absorption fine structure (EXAFS), as shown in Fig. 1c clearly represents the change in surrounding environment of iridium in mixed composites than in IrO_2. The first high intense peak corresponds to Ir-O bond in its IrO_6 coordination. A slight enlargement of this bond was observed in case of mixed composites on
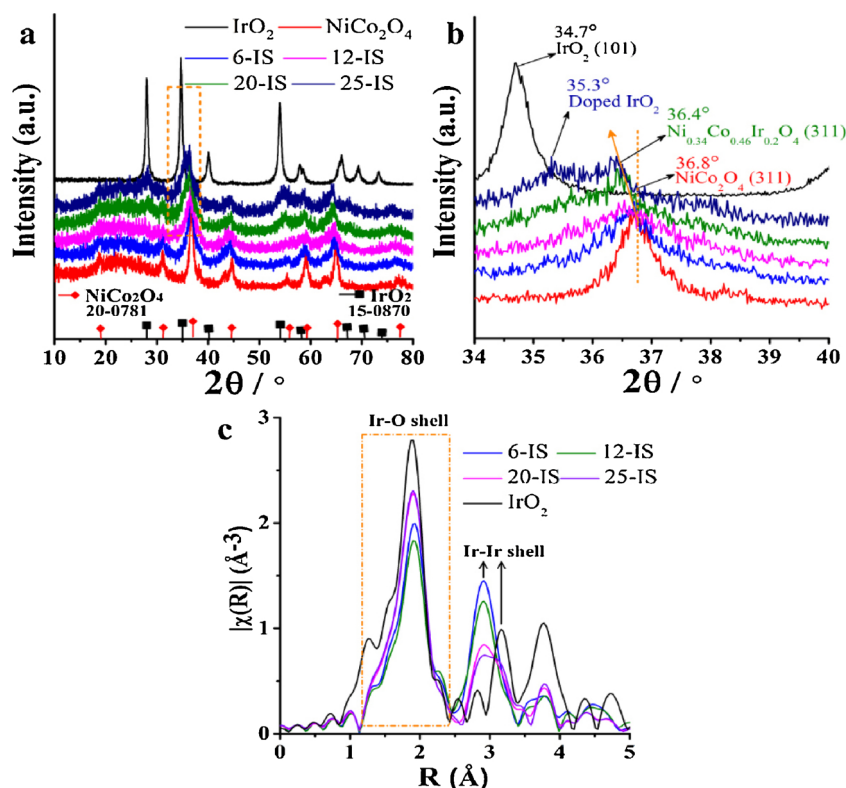

Fig. 1. (a) XRD spectra of IrO_2, $NiCo_2O_4$ and Ir doped $NiCo_2O_4$ composites. (b) Selected angle range showing deviation from the plane (311) of $NiCo_2O_4$ due to iridium doping and (c) Fourier transforms of k^3 normalized Ir-LIII edge EXAFS of IrO_2 and Ir doped $NiCo_2O_4$ composites.
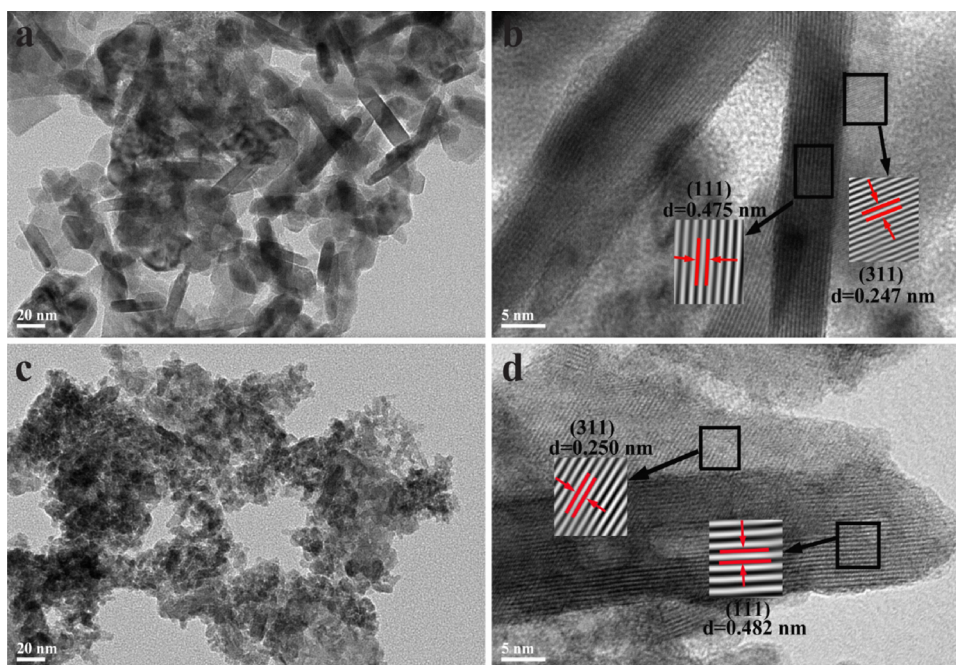
Fig. 2. (a) and (b) TEM images of $NiCo_2O_4$, (c) and (d) TEM images of 20-IS.

comparing to IrO_2. This bond elongation along the plane corresponding to apical O of IrO_6 octahedra indicates significant lattice distortion on being substituted in different structure. Followed by the Ir−O bond peak the next appearing peak is associated to Ir−Ir that appears almost at 3.16 Å in IrO_2. Whereas, according to literature for spinel nickel cobaltite this peak appears at a bond length of approximately 2.85 Å [26,27]. For all the prepared doped composites this peak lied much closer to the latter with slight increase in the bond length. Firstly, the increase in bond length was well in consistence to XRD results of observed shift in diffraction angle towards lower value confirming substitution of a specie with higher radius. Secondly, much reduced Ir−Ir bond length in these composites than in IrO_2 confirmed the presence of iridium in a crystal system other than rutile. All the composites had this feature very different from pure IrO_2 spectra and the peak position indicated an approximate Ir−Ir bond length of 2.9 Å being very alike to that in spinel nickel cobaltite. Whereas, clear existence of both spinel and rutile phases in 25-IS composite was confirmed by its Ir−Ir peak showing asymmetrical broadness than rest composites tending towards higher bond length as in IrO_2. The observed structural variations from XRD and Ir-L_{III} EXAFS confirms successful iridium doping but to a certain limitation of almost 20 mol%.

3.2. Electrocatalytic activity and durability

The evident lattice modification within the crystal system due to elongation of Ir−O and reduction of Ir−Ir bond length must accompany, OER beneficial, corresponding variations in electrocatalytic properties [28,29]. To observe this effect, for iridium doped nickel cobaltite, all the fabricated composites were subjected as an anode material to three electrode chemical cell in acidic media. It is observed from the Fig. 3a that pure nickel cobaltite rendered no OER catalytic response at any value of applied voltage in acidic solution. Whereas, an increasing trend towards OER activity is observed for all the doped composites with increasing percentage of iridium content till its presence of 20 mol%. Later on, a drop in activity was observed for 25-IS due to display of slightly larger onset potential than 20-IS that well attributes to the adequate presence of iridium in both spinel and rutile phases as seen earlier; indicating intrinsic difference between the active sites of both phases. A tilted behavior of 12-IS LSV curve is seen after potential value

of 1 V. This can be ascribed to cobalt oxidation at surface due to insufficient iridium content in the composite, which has been earlier observed for studies on IrO_2/Co_3O_4 and Ag doped Co_3O_4 [30,31]. At a potential value of 1.55 V (RHE) the exhibited current densities were $13.68 \, mA \, cm^{-2}$, $28.27 \, mA \, cm^{-2}$, $9.51 \, mA. \, cm^{-2}$ and $1.42 \, mA \, cm^{-2}$ for 25-IS, 20-IS, 12-IS and 6-IS, respectively, where pure IrO_2 exhibited just $4.24 \, mA \, cm^{-2}$. The best performing composite, 20-IS, also showed up as the best mass specific OER performer upon displaying more than 15 folds enhancement in activity compared to IrO_2 at an overpotential of just 320 mV. Moreover, the current density of $10 \, mA \, cm^{-2}$, contemplated as useful index to solar fuel synthesis, was acquired by 20-IS at an overpotential value of just 280 mV; marking as one of the best among the known iridium based water splitting catalyst in acidic media [32,33]. In Table 1 the OER activity of 20-IS is compared with the performance of recently reported iridium based materials in acidic medium. Comparison shows noticeable activity of 20-IS to other iridium based composites. Roots for such an enhancement in OER activity emerge either from a less positive potential (related to a higher exchange current density j_o) and a smaller tafel slope (indicating a change in the mechanism); both of these parameters constitute the improved kinetics. The performance of composite 20-IS resulted as combinatorial effect from the improvement of these both sectors. It possessed a lower onset potential as shown in Fig. 3c, almost 190 mV that being closer to thermodynamically known 123 mV, and a tafel slope of $40.4 \, mV \, dec^{-1}$, being much steeper than IrO_2 possessing $68 \, mV \, dec^{-1}$ for an onset potential of 260 mV that is quite in agreement to previously conducted studies [34,35]. The tafel slopes of other contrastive samples in study are presented in Fig. S6. Such reduction in value of tafel slope can be attributed to the change of OER mechanism [36]. Additionally, composite 20-IS also possessed higher electrochemical surface area of $182 \, m^2 \, g^{-1}$, evaluated on extracting the electrochemical double layer capacitance (C_d) [37,38], than IrO_2 possessing $115 \, m^2 \, g^{-1}$. The specific capacitance for IrO_2 was taken as $0.35 \, mF \, cm^{-2}$ as previously reported, while considering the outer electrode surface [39]. Furthermore, the obtained Electrochemical Impedance Spectroscopy (EIS) presented in Fig. S7, reveals the best charge transport efficiency for 20-IS. Maximum resistance was observed for pure $NiCo_2O_4$ that well supports its inert behavior in acid media as presented Fig. 3a. Iridium doping in spinel gradually improved the conductance, which appeared maximum for 20-
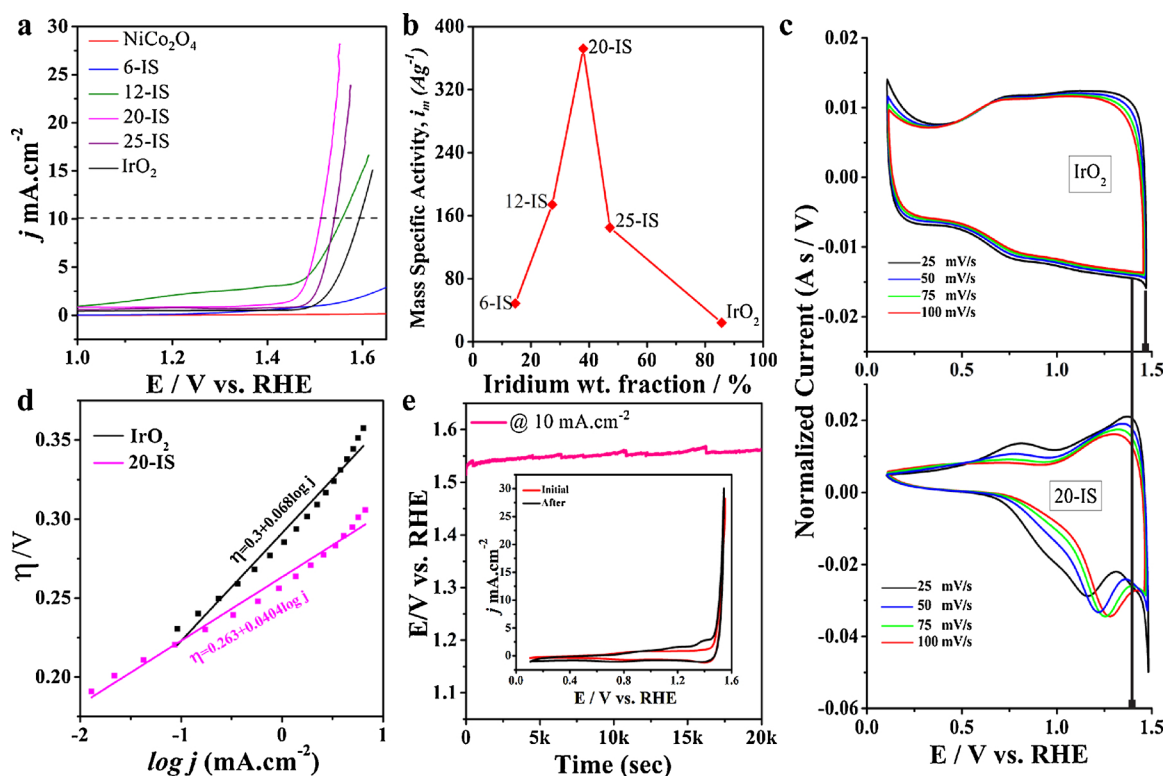
Fig. 3. (a) Linear sweep voltammetery curves with *iR* correction for the OER process of IrO_2, $NiCo_2O_4$ and Ir doped $NiCo_2O_4$ composites in the acidic solution (0.1 M $HClO_4$). (b) Mass specific activity of IrO_2 and all Ir doped $NiCo_2O_4$ composites at 1.55 V vs. RHE. (c) Normalized CV curves with different scan rates for 20-IS and IrO_2 in 0.1 M $HClO_4$. (d) Tafel plots of IrO_2 and 20-IS. (e) Chronoamperometric curves at the constant current density 10 mA/cm². Insert shows the polarization curves for 20-IS initial and after the chronoamperometric experiments.

Table 1

OER performance comparison of iridium doped nickel cobaltite with other Ir based materials in acidic medium.

catalysts	solution	overpotential (V) at 10 mA cm⁻² vs RHE	Tafel slope (mV dec⁻¹)	reference no.
$Ni_{0.34}Co_{0.46}Ir_{0.2}O_8$	0.1 M $HClO_4$	0.280	40	This work
Ir/Co4N	0.5 M H_2SO_4	0.319	67	[42]
$Ir_{0.3}Mo_{0.7}O_8$	0.1 M $HClO_4$	0.345	57	[43]
$RuIrCoO_x$	0.5 M H_2SO_4	0.394	70	[44]
$Ir_{0.7}Ni_{0.3}O_{2-y}$	0.5 M H_2SO_4	0.335	57	[45]
$IrO_2 - Ta_2O_5$ oxide	0.5 M H_2SO_4	0.362	59	[46]
$Ir_{0.7}Co_{0.3}O_x$	0.5 M H_2SO_4	0.33	40	[47]
$Bi_2Ir_2O_7$	1 M H_2SO_4	0.365	45	[48]
$0.5IrO2 - 0.5SiO2$	0.5 M H_2SO_4	0.322	80	[49]
$Ir_{0.4}Mn_{0.6}O_8$	0.1 M H_2SO_4	0.285	40	[50]
$Ir_2Sn_1O_x$	0.5 M $HClO_4$	0.335	65	[51]

IS followed by a decrease for 25-IS that can be attributed again to the adequate presence of iridium in both phases. Since previous reports show influence of host structures on electronic conductance, therefore for 25-IS the exhibited plot probably involves the influence of iridium sites from both phases i.e., rutile and spinel [37,40]. The intrinsic improvement of spinel incorporated iridium sites was also observed from the lower product values of R$_{ct}$ and C$_d$ indicating a rise in intrinsic catalytic activity as presented in Fig. S8 [41]. The best performing composite, 20-IS was also subjected to a series of temperature-dependent electrocatalytic tests as shown in Fig. S9. Other than room temperature (25 °C) the current density of prepared electrodes was also measured at 40 °C, 50 °C and 60 °C. An immediate improvement in activity was observed at 40 °C. Later at higher temperature values of 50 °C and 60 °C no further improvement was observed. The rise in activity

compared to room temperature can be attributed to the quicker escape of oxygen bubbles from electrode surface (after having enough heat energy compared to room temperature operation) that eventually frees the bubbles veiled electrode area for further interaction.

Along with OER catalytic activity, durability of the catalyst holds prime importance and a reason for iridium inclusion to confront the harsh acidic environment. All the precious metal doped spinel composites were subjected to chronoamperometric tests for 20,000 s and 40,000 s at a current density of 10 mA cm⁻² in an acidic solution of 0.1 M $HClO_4$ as presented in Figs. 3e and S10. Iridium at mol% content of 20, in 20-IS, was found as the minimal content required to withstand the corrosive environment. As, composites with lower iridium content couldn't dissipate the set current density at stable potential values. Where, 20-IS maintained a stable value of potential for the set current density. Interestingly, a slight increased value of current density was observed from 28.4 to 30.2 mA cm⁻² for the before and after conducted linear sweep voltammetry to durability test of 20,000 s. Such fractional enhancement in OER activity is attributed to the unveiling of intermittent iridium at top surface layers, after leaching of confronting nickel or cobalt, to the electrolytic media [14,52,53]. The excessive leaching of nickel and cobalt was confirmed on obtaining concentration of metallic leachates in electrolyte via inductively coupled plasma mass spectrometry (ICP-MS) analysis after a long durability test of 20,000 s. The concentration of nickel and cobalt was 0.35 mg/L and 0.24 mg/L, respectively, whereas, iridium showed just 0.024 mg/L. It means that after the stability test composites surface mostly comprised noble metal. Additionally, the conducted XRD analysis after the OER process as shown in Figs. S11 and S12 presented a peak at 35.5° arising from the neighbor of nickel cobaltite peak with indices (311). The diffraction angle of this observed peak lies between the diffraction angles of 34.8° and 36.72 of rutile IrO_2 plane (101) and of spinel $NiCO_2O_4$ plane (311), respectively. These results infer formation of iridium enriched layers of IrO_x, responsible in exhibition of composites robust behavior towards
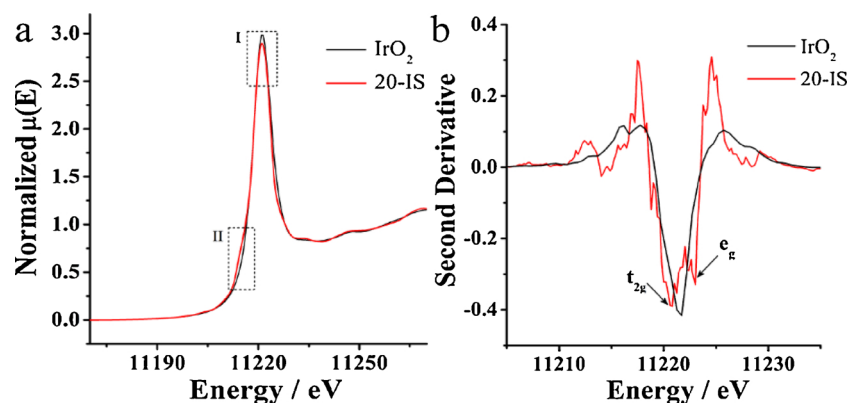
Fig. 4. (a) The Ir LIII-edge XANES spectra for 20-IS and IrO$_2$. (b) Second derivatives of Ir-LIII edge XANES spectra for 20-IS and IrO$_2$.

harsh acidic environment [14,52].

3.3. Electronic characterization of iridium sites by Ir L_{111}-edge XANES and XPS study

Iridium's presence in other than rutile structure along with superb OER catalytic performance indicates expedient modulations in electronic structure of the precious metal. To corroborate this notion the data for Ir L_{111}-edge XANES in both IrO$_2$ and 20-IS was acquired. As it best determines the electronic structure corresponding to local site occupation and to covalency in bonding character for being sensitive to the crystal field effect, the spin state, and the oxidation state. The exhibited shape and energy position of adsorption intensity, called as "the white line" plays an important role in reflecting the local symmetry and oxidation state of iridium in composites. Herein, there appeared almost no change in the position of the white line for both composites under consideration inferring a similar oxidation state of iridium in rutile IrO$_2$ and in doped spinel, 20-IS. Whereas, a reduction in intensity of white line and appearance of shake down peak was observed for 20-IS, shown in Fig. 4 as 1 and 11 respectively, relative to IrO$_2$. Reduced intensity depicts electronic transitions in Ir-5d states and the near edge peak results due to change in crystal symmetry that being in consistent to earlier observed reduction in Ir—Ir and elongation in Ir—O bond lengths, respectively [17]. Hence, both observed features from Fig. 4 confirm the consequent electronic modulations in association to distortion in crystal symmetry upon iridium doping [54]. The second derivative of Ir L_{111}-edge XANES spectra showed more clearly the electronic transitions of Ir-5d electrons as for doped composites there appeared double peak corresponding to t$_{2g}$ and e$_g$ orbital transitions unlike IrO$_2$ possessing a single peak representing t$_{2g}^5$ and e$_g^0$. Earlier conducted studies have confirmed that partial occupation of e$_g$ orbitals, as observed here, lead to a higher OER activity as spin orbital occupation correlates to surface oxygen bond energy. The increase in occupation number correspondingly weakens the interaction between the surface site and adsorbed oxygen species that ultimately improves the OER kinetics [55,56].

To obtain the chemical oxidation state information of metallic species present in synthesized composite X ray photoelectron spectroscopic (XPS) analysis was conducted. The obtained results showed the surface presence of all the elements in current study. Fig. 5 shows the XPS spectra of Co, Ni, Ir, and O in the pure oxides of IrO$_2$ and NiCo$_2$O$_4$ along with their presence in 20-IS. In part b of Fig. 5, the spectra from core 2p level of cobalt show the presence of two spin orbit doublets, Co-2p$_{3/2}$ and Co-2p$_{1/2}$, at a difference of approximately 15.1 eV that is in well agreement to previous studies [57,58]. Moreover, the spectrum profile of Co-2p in doped and undoped nickel cobaltite is analogous to that in Co$_3$O$_4$ [31,59,60]. However, it is hard to determine the exact oxidation states of Co just from the main 2p peaks binding energy position and profile due to alike trails in various oxidation states. On

contrary, for nickel the spectrum line shape along with two main peaks at 855.5 eV and 872.9 eV were well attributed to its +2 oxidation state [61,62] Nevertheless, consideration of satellite peaks for cobalt in this regard gives valuable indication. Appearance of low intense satellite peaks at a binding energy difference of 6 eV and 9–10 eV from the main Co-2p$_{3/2}$ peak show presence of +3 and +2 cobalt oxidation state in both samples as indicated by S1 and S2 in Fig. 5b. A relatively decreased intensity of S2 is observed in case of doped composite than undoped nickel cobaltite. This decrease might have occurred in correspondence to partial iridium occupation of octahedral sites rather than Co +3 [63]. Structural modulation due to iridium inclusion is also depicted from the Ni-2p spectrum. The intensity ratio between the main Ni-2p$_{3/2}$ peak at 855.5 eV and a peak adjoining to it at 853.6 eV have been pointed out earlier as a function of local environment contiguous to nickel atoms [64]. Change in this ratio as observed from the Fig. 5b clearly indicate the iridium substituting cobalt at neighboring octahedral sites of nickel atoms in doped composites of current study. Iridium, as being more electronegative than cobalt, upon substitution is further suspected to induce polarization for the shared electrons. In perspective to such suspicion, from the Fig. 5d showing O 1s spectra, a shift towards higher binding energy was observed by 0.25 eV in 20-IS, suggesting the polarization of metal-oxygen shared electrons away from oxygen atoms [65]. Moreover, the labeled peak P2 regarded as oxygen vacancy contributing was found relatively intense in 20-IS [66–68]. These vacancies became more intense after the OER activity as shown in Figure S14. Where, generation of oxygen vacancies are as known to be accompanied with electronic modulations for doped composites resulting due to neutrality maintenance of the host crystal structure. These vacancies in further lead to pronounced metallic character of active catalytic species that eventually improves the OER kinetics. As, in this study iridium's core 4f spectrum obtained from 20-IS presents broadened and more asymmetrical peaks of Ir-4f$_{7/2}$ and Ir-4f$_{5/2}$ relative to that of IrO$_2$. Increase in asymmetry is related to the enhancement in metallic character, whereas the peak broadening indicates the change in local surrounding of iridium atoms being different in nature due to perturbation caused by the existing host metallic species [69]. Additionally, a weak peak at a binding energy of 59.9 eV was observed, which corresponds to metallic iridium 4f$_{7/2}$ [70]. Moreover, an increase of 0.2 eV was observed in binding energy for Ir-4f$_{7/2}$ in 20-IS than in IrO$_2$ as a result of more electronegative nature of iridium than the counterparts.

All the performed characterizations well depicted the deterioration of the spinel structure upon iridium inclusion and the associated electronic modulations. Among all physical characterizations, the Ir-L_{III} edge presented a dramatic reduction of Ir—Ir bond length. Its shortening has been proven beneficial in current study for enhancing the electrocatalytic performance of confronting iridium centers along with substantial reduction of noble metal than previously reported for hollandite structures [16,17]. The observed shortening leads to a compressive stress along the c-axis that eventually reduces the c/a ratio and distorts
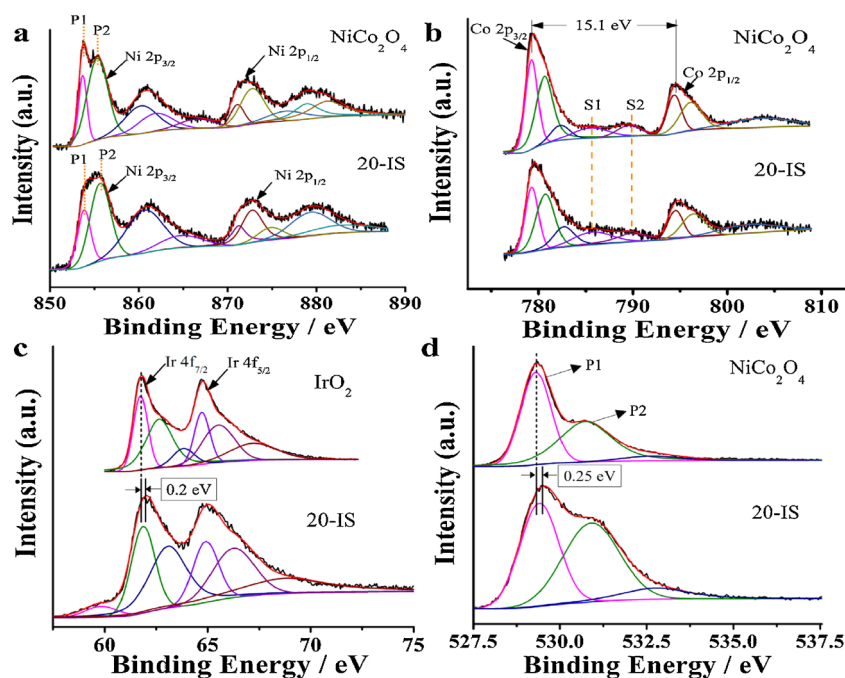
Fig. 5. XPS spectra of (a) Ni-2p and (b) Co-2p in NiCo$_2$O$_4$ and 20-IS. Where (c) and (d) showing spectra of Ir-4f and O-1s in IrO$_2$ and NiCo$_2$O$_4$ respectively comparative to 20-IS.

the iridium octahedral units leading to Jahn Teller's effect responsible in positively influencing the OER activity [11,16,29,71]. Future exploration of such host structures in further exploiting edge-sharing IrO$_6$ octahedra distance can to lead more advancements in economical and efficient OER catalysis.

4. Conclusion

In summary, we report a facile engineering approach for effective utilization of iridium metal to conduct electrocatalytic water splitting in acidic environment. NiCo$_2$O$_4$ as suitable non noble host structure with high OER structural descriptor ratio was chosen for limited inclusion of noble iridium, at almost 20% mol fraction of composite, to robustly confront the water splitting. Various employed characterizations techniques confirmed, OER beneficial, novel existence of iridium in this spinel structure. Over 15 folds enhancement in mass specific activity was obtained relative to pure IrO$_2$. The superb OER performance at expense of limited iridium was attributed to the efficient electronic tuning of iridium due to shortened IrO$_6$ octehedra inter distance after iridium's incorporation into spinel structure. Hence, current implemented approach, presents a significant enhancement in current density whilst limited iridium consumption that would open new avenues for efficient usage of precious elements to economize the overall water splitting process.

Appendix A. Supplementary data

Supplementary material related to this article can be found, in the online version, at doi:https://doi.org/10.1016/j.apcatb.2018.10.041.

References

[1] G.K. Lilik, H. Zhang, J.M. Herreros, D.C. Haworth, A.L. Boehman, Hydrogen assisted diesel combustion, Int. J. Hydrogen Energy 35 (2010) 4382–4398.
[2] H. Zhou, Y. Wang, H. Li, P. He, The development of a new type of rechargeable batteries based on hybrid electrolytes, ChemSusChem 3 (2010) 1009–1019.
[3] J. Pettersson, B. Ramsey, D. Harrison, A review of the latest developments in electrodes for unitised regenerative polymer electrolyte fuel cells, J. Power Sources 157 (2006) 28–34.
[4] A.Z. Weber, M.M. Mench, J.P. Meyers, P.N. Ross, J.T. Gostick, Q. Liu, Redox flow batteries: a review, J. Appl. Electrochem. 41 (2011) 1137–1164.
[5] J. Herranz, J. Durst, E. Fabbri, A. Patru, X. Cheng, A.A. Permyakova, T.J. Schmidt, Interfacial effects on the catalysis of the hydrogen evolution, oxygen evolution and CO 2-reduction reactions for (co-) electrolyzer development, Nano Energy (2016).
[6] J.K. Nørskov, T. Bligaard, J. Rossmeisl, C.H. Christensen, Towards the computational design of solid catalysts, Nat. Chem. 1 (2009) 37–46.
[7] S. Cherevko, A.R. Zeradjanin, A.A. Topalov, N. Kulyk, I. Katsounaros, K.J. Mayrhofer, Dissolution of noble metals during oxygen evolution in acidic media, ChemCatChem 6 (2014) 2219–2223.
[8] D.F. Abbott, D. Lebedev, K. Waltar, M. Povia, M. Nachtegaal, E. Fabbri, C. Copéret, T.J. Schmidt, Iridium oxide for the oxygen evolution reaction: correlation between particle size, morphology, and the surface hydroxo layer from operando XAS, Chem. Mater. 28 (2016) 6591–6604.
[9] H.N. Nong, H.S. Oh, T. Reier, E. Willinger, M.G. Willinger, V. Petkov, D. Teschner, P. Strasser, Oxide-supported IrNiOx core–shell particles as efficient, cost-effective, and stable catalysts for electrochemical water splitting, Angew. Chem. Int. Ed. 54 (2015) 2975–2979.
[10] A. Papaderakis, N. Pliatsikas, C. Prochaska, G. Vourlias, P. Patsalas, D. Tsiplakides, S. Balomenou, S. Sotiropoulos, Oxygen evolution at IrO2 shell–Ir–Ni core electrodes prepared by galvanic replacement, J. Phys. Chem. C 120 (2016) 19995–20005.
[11] W. Sun, Y. Song, X.-Q. Gong, L.-m. Cao, J. Yang, An efficiently tuned d-orbital occupation of IrO2 by doping with Cu for enhancing the oxygen evolution reaction activity, Chem. Sci. 6 (2015) 4993–4999.
[12] R.G. González-Huerta, G. Ramos-Sánchez, P.B. Balbuena, Oxygen evolution in Co-doped RuO2 and IrO2: experimental and theoretical insights to diminish electrolysis overpotential, J. Power Sources 268 (2014) 69–76.
[13] W.Q. Zaman, Z. Wang, W. Sun, Z. Zhou, M. Tariq, L. Cao, X.-Q. Gong, J. Yang, Ni–Co codoping breaks the limitation of single-metal-doped IrO2 with higher oxygen evolution reaction performance and less iridium, ACS Energy Lett. (2017) 2786–2793.
[14] D. Lebedev, M. Povia, K. Waltar, P.M. Abdala, I.E. Castelli, E. Fabbri, M.V. Blanco, A. Fedorov, C. Copéret, N. Marzari, Highly active and stable iridium pyrochlores for oxygen evolution reaction, Chem. Mater. (2017).
[15] O. Diaz-Morales, S. Raaijman, R. Kortlever, P.J. Kooyman, T. Wezendonk, J. Gascon, W. Fu, M.T. Koper, Iridium-based double perovskites for efficient water oxidation in acid media, Nat. Commun. 7 (2016) 12363.
[16] E. Willinger, C. Massué, R. Schlögl, M.-G. Willinger, Identifying key structural features of IrOx water splitting catalysts, J. Am. Chem. Soc. (2017).
[17] W. Sun, Y. Song, X.-Q. Gong, L.-m. Cao, J. Yang, Hollandite structure K x ≈ 0.25

IrO2 catalyst with highly efficient oxygen evolution reaction, ACS Appl. Mater. Interfaces 8 (2015) 820–826.

[18] R. BRCNR, Transition Metal Oxides: Structure, Properties, and Synthesis of Ceramic Oxides, Wiley–VCH, New York and Weinheim, 1998.

[19] M. Lenglet, R. Guillamet, J. Dürr, D. Gryffroy, R. Vandenberghe, Electronic structure of NiCo 2O4 by XANES, EXAFS and 61 Ni Mössbauer studies, Solid State Commun. 74 (1990) 1035–1039.

[20] X. Shi, S.L. Bernasek, A. Selloni, Oxygen deficiency and reactivity of spinel NiCo2O4 (001) surfaces, J. Phys. Chem. C 121 (2017) 3929–3937.

[21] L. Liu, H. Zhang, L. Fang, Y. Mu, Y. Wang, Facile preparation of novel dandelion-like Fe-doped NiCo2O4 microspheres@nanomeshes for excellent capacitive property in asymmetric supercapacitors, J. Power Sources 327 (2016) 135–144.

[22] S. Krehula, G. Štefanić, K. Zadro, L. Kratofil Krehula, M. Marciuš, S. Musić, Synthesis and properties of iridium-doped hematite (α-Fe2O3), J. Alloys. Compd. 545 (2012) 200–209.

[23] K.-L. Yan, X. Shang, Z. Li, B. Dong, X. Li, W.-K. Gao, J.-Q. Chi, Y.-M. Chai, C.-G. Liu, Ternary mixed metal Fe-doped NiCo2O4 nanowires as efficient electrocatalysts for oxygen evolution reaction, Appl. Surf. Sci. 416 (2017) 371–378.

[24] T. Swathi, G. Buvaneswari, Application of NiCo2O4 as a catalyst in the conversion of p-nitrophenol to p-aminophenol, Mater. Lett. 62 (2008) 3900–3902.

[25] S.-K. Chang, K.-T. Lee, Z. Zainal, K.-B. Tan, N.A. Yusof, W.M.D.W. Yusoff, J.-F. Lee, N.-L. Wu, Structural and electrochemical properties of manganese substituted nickel cobaltite for supercapacitor application, Electrochim. Acta 67 (2012) 67–72.

[26] A.V. Chadwick, S.L. Savin, S. Fiddy, R. Alcantara, D. Fernández Lisbona, P. Lavela, G.F. Ortiz, J.L. Tirado, Formation and oxidation of nanosized metal particles by electrochemical reaction of Li and Na with NiCo2O4: X-ray absorption spectroscopic study, J. Phys. Chem. C 111 (2007) 4636–4642.

[27] J.F. Marco, J.R. Gancedo, M. Gracia, J.L. Gautier, E.I. Ríos, H.M. Palmer, C. Greaves, F.J. Berry, Cation distribution and magnetic structure of the ferrimagnetic spinel NiCo2O4, J. Mater. Chem. 11 (2001) 3087–3093.

[28] W. Sun, J.-Y. Liu, X.-Q. Gong, W.-Q. Zaman, L.-M. Cao, J. Yang, OER activity manipulated by IrO6 coordination geometry: an insight from pyrochlore iridates, Sci. Rep. 6 (2016) 38429.

[29] T. Reier, Z. Pawolek, S. Cherevko, M. Bruns, T. Jones, D. Teschner, Sr. Selve, A. Bergmann, H.N. Nong, R. Schlögl, Molecular insight in structure and activity of highly efficient, low-Ir Ir–Ni oxide catalysts for electrochemical water splitting (OER), J. Am. Chem. Soc. 137 (2015) 13031–13040.

[30] W. Valenzuela Barrientos, L.R.-T. Gómez, Preparación, caracterización y evaluación de la estabilidad electroquímica de electrodos Ti/Co3O4-xIrO2, Revista de la Sociedad Química del Perú 81 (2015) 148–159.

[31] K.-L. Yan, J.-Q. Chi, J.-Y. Xie, B. Dong, Z.-Z. Liu, W.-K. Gao, J.-H. Lin, Y.-M. Chai, C.-G. Liu, Mesoporous Ag-doped Co3O4 nanowire arrays supported on FTO as efficient electrocatalysts for oxygen evolution reaction in acidic media, Renew. Energy 119 (2018) 54–61.

[32] S.D. Ghadge, P.P. Patel, M.K. Datta, O.I. Velikokhatnyi, R. Kuruba, P.M. Shanthi, P.N. Kumta, Fluorine substituted (Mn, Ir) O2: F high performance solid solution oxygen evolution reaction electro-catalysts for PEM water electrolysis, RSC Adv. 7 (2017) 17311–17324.

[33] M. Tahir, L. Pan, F. Idrees, X. Zhang, L. Wang, J.-J. Zou, Z.L. Wang, Electrocatalytic oxygen evolution reaction for energy conversion and storage: a comprehensive review, Nano Energy (2017).

[34] A. Marshall, B. Børresen, G. Hagen, M. Tsypkin, R. Tunold, Hydrogen production by advanced proton exchange membrane (PEM) water electrolysers—reduced energy consumption by improved electrocatalysts, Energy 32 (2007) 431–436.

[35] M.E. Lyons, S. Floquet, Mechanism of oxygen reactions at porous oxide electrodes. Part 2–oxygen evolution at RuO2, IrO2 and IrxRu1-xO2 electrodes in aqueous acid and alkaline solution, J. Chem. Soc. Faraday Trans. 13 (2011) 5314–5335.

[36] T. Reier, H.N. Nong, D. Teschner, R. Schlögl, P. Strasser, Electrocatalytic oxygen evolution reaction in acidic environments–reaction mechanisms and catalysts, Adv. Energy Mater. 7 (2017) 1601275.

[37] W. Sun, L. Cao, J. Yang, Conversion of inert cryptomelane-type manganese oxide into a highly efficient oxygen evolution catalyst via limited Ir doping, J. Mater. Chem. A (2016).

[38] K.-L. Yan, J.-Q. Chi, Z.-Z. Liu, B. Dong, S.-S. Lu, X. Shang, W.-K. Gao, Y.-M. Chai, C.-G. Liu, Coupling Ag-doping and rich oxygen vacancies in mesoporous NiCoO nanorods supported on nickel foam for highly efficient oxygen evolution, Inorg. Chem. Front. 4 (2017) 1783–1790.

[39] C.C.L. McCrory, S. Jung, J.C. Peters, T.F. Jaramillo, Benchmarking heterogeneous electrocatalysts for the oxygen evolution reaction, J. Am. Chem. Soc. 135 (2013) 16977–16987.

[40] G.A.M. Ali, M.M. Yusoff, E.R. Shaaban, K.F. Chong, High performance MnO2 nanoflower supercapacitor electrode by electrochemical recycling of spent batteries, Ceram. Int. 43 (2017) 8440–8448.

[41] A. Papaderakis, D. Tsiplakides, S. Balomenou, S. Sotiropoulos, Electrochemical impedance studies of IrO2 catalysts for oxygen evolution, J. Electroanal. Chem. 757 (2015) 216–224.

[42] B.M. Tackett, W. Sheng, S. Kattel, S. Yao, B. Yan, K.A. Kuttiyiel, Q. Wu, J.G. Chen, Reducing iridium loading in oxygen evolution reaction electrocatalysts using core–shell particles with nitride cores, ACS Catal. 8 (2018) 2615–2621.

[43] M. Tariq, W.Q. Zaman, W. Sun, Z. Zhou, Y. Wu, L.-m. Cao, J. Yang, Unraveling the beneficial electrochemistry of IrO2/MoO3 hybrid as a highly stable and efficient oxygen evolution reaction catalyst, ACS Sustain. Chem. Eng. 6 (2018) 4854–4862.

[44] J. Corona-Guinto, L. Cardeño-García, D. Martínez-Casillas, J.M. Sandoval-Pineda,

[45] P. Tamayo-Meza, R. Silva-Casarin, R. González-Huerta, Performance of a PEM electrolyzer using RuIrCoOx electrocatalysts for the oxygen evolution electrode, Int. J. Hydrogen Energy 38 (2013) 12667–12673.

[45] S. Xu, Y. Liu, J. Tong, W. Hu, Q. Xia, Iridium–nickel composite oxide catalysts for oxygen evolution reaction in acidic water electrolysis, Russ. J. Electrochem. 52 (2016) 1021–1031.

[46] J.-M. Hu, J.-Q. Zhang, C.-N. Cao, Oxygen evolution reaction on IrO2-based DSA® type electrodes: kinetics analysis of Tafel lines and EIS, Int. J. Hydrogen Energy 29 (2004) 791–797.

[47] W. Hu, H. Zhong, W. Liang, S. Chen, Ir-surface enriched porous Ir-Co oxide hierarchical architecture for high performance water oxidation in acidic media, ACS Appl. Mater. Interfaces 6 (2014) 12729–12736.

[48] K. Sardar, S.C. Ball, J.D. Sharman, D. Thompsett, J.M. Fisher, R.A. Smith, P.K. Biswas, M.R. Lees, R.J. Kashtiban, J. Sloan, Bismuth iridium oxide oxygen evolution catalyst from hydrothermal synthesis, Chem. Mater. 24 (2012) 4192–4200.

[49] J.-J. Zhang, J.-M. Hu, J.-Q. Zhang, C.-N. Cao, IrO2-SiO2 binary oxide films: geometric or kinetic interpretation of the improved electrocatalytic activity for the oxygen evolution reaction, Int. J. Hydrogen Energy 36 (2011) 5218–5226.

[50] Z. Zhou, W.Q. Zaman, W. Sun, L. Cao, M. Tariq, J. Yang, Cultivating crystal lattice distortion in IrO2 via coupling with MnO2 to boost oxygen evolution reaction with high intrinsic activity, Chem. Commun. (2018).

[51] W. Lu, P. Yuan, F. Wei, K. Cheng, W. Li, Y. Zhou, W. Zheng, G. Zhang, Porous Ir-Sn binary oxide nanorod assembly as an efficient electrocatalyst for water oxidation, Int. J. Electrochem. Sci. 13 (2018) 3235–3245.

[52] L.C. Seitz, C.F. Dickens, K. Nishio, Y. Hikita, J. Montoya, A. Doyle, C. Kirk, A. Vojvodic, H.Y. Hwang, J.K. Norskov, A highly active and stable IrOx/SrIrO3 catalyst for the oxygen evolution reaction, Science 353 (2016) 1011–1014.

[53] L. Wang, V.A. Saveleva, S. Zafeiratos, E.R. Savinova, P. Lettenmeier, P. Gazdzicki, A.S. Gago, K.A. Friedrich, Highly active anode electrocatalysts derived from electrochemical leaching of Ru from metallic Ir 0.7 Ru 0.3 for proton exchange membrane electrolyzers, Nano Energy 34 (2017) 385–391.

[54] J.-H. Choy, D.-K. Kim, S.-H. Hwang, G. Demazeau, D.-Y. Jung, XANES and EXAFS studies on the Ir−O bond covalency in ionic iridium perovskites, J. Am. Chem. Soc. 117 (1995) 8557−8566.

[55] J. Suntivich, K.J. May, H.A. Gasteiger, J.B. Goodenough, Y. Shao-Horn, A perovskite oxide optimized for oxygen evolution catalysis from molecular orbital principles, Science 334 (2011) 1383–1385.

[56] A. Vojvodic, J.K. Nørskov, Optimizing perovskites for the water-splitting reaction, Science 334 (2011) 1355–1356.

[57] D. Barreca, C. Massignan, S. Daolio, M. Fabrizio, C. Piccirillo, L. Armelao, E. Tondello, Composition and microstructure of cobalt oxide thin films obtained from a novel cobalt (II) precursor by chemical vapor deposition, Chem. Mater. 13 (2001) 588–593.

[58] A. Gulino, G. Fiorito, I. Fragalà, Deposition of thin films of cobalt oxides by MOCVD, J. Mater. Chem. 13 (2003) 861–865.

[59] M.C. Biesinger, B.P. Payne, A.P. Grosvenor, L.W. Lau, A.R. Gerson, R.S.C. Smart, Resolving surface chemical states in XPS analysis of first row transition metals, oxides and hydroxides: Cr, Mn, Fe, Co and Ni, Appl. Surf. Sci. 257 (2011) 2717–2730.

[60] K.-L. Yan, J.-F. Qin, J.-H. Lin, B. Dong, J.-Q. Chi, Z.-Z. Liu, F.-N. Dai, Y.-M. Chai, C.-G. Liu, Probing the active sites of Co3O4 for the acidic oxygen evolution reaction by modulating the Co2+/Co3+ ratio, J. Mater. Chem. A 6 (2018) 5678–5686.

[61] A.P. Grosvenor, M.C. Biesinger, R.S.C. Smart, N.S. McIntyre, New interpretations of XPS spectra of nickel metal and oxides, Surf. Sci. 600 (2006) 1771–1779.

[62] J. Ji, L.L. Zhang, H. Ji, Y. Li, X. Zhao, X. Bai, X. Fan, F. Zhang, R.S. Ruoff, Nanoporous Ni (OH) 2 thin film on 3D ultrathin-graphite foam for asymmetric supercapacitor, ACS Nano 7 (2013) 6237–6243.

[63] W. Wei, W. Chen, D.G. Ivey, Rock salt-spinel structural transformation in anodically electrodeposited Mn–Co–O nanocrystals, Chem. Mater. 20 (2008) 1941–1947.

[64] D. Alders, F. Voogt, T. Hibma, G. Sawatzky, Nonlocal screening effects in 2p x-ray photoemission spectroscopy of NiO (100), Phys. Rev. B 54 (1996) 7716.

[65] M.C. Biesinger, L.W. Lau, A.R. Gerson, R.S.C. Smart, The role of the Auger parameter in XPS studies of nickel metal, halides and oxides, J. Chem. Soc. Faraday Trans. 14 (2012) 2434–2442.

[66] D. Yan, W. Wang, X. Luo, C. Chen, Y. Zeng, Z. Zhu, NiCo2O4 with oxygen vacancies as better performance electrode material for supercapacitor, Chem. Eng. J. 334 (2018) 864–872.

[67] V.H. Nguyen, C. Lamiel, J.-J. Shim, Mesoporous 3D graphene@NiCo2O4 arrays on nickel foam as electrodes for high-performance supercapacitors, Mater. Lett. 170 (2016) 105–109.

[68] S. Wei, X. Wang, B. Zhang, M. Yu, Y. Zheng, Y. Wang, J. Liu, Preparation of hierarchical core-shell C@NiCo2O4@Fe3O4 composites for enhanced microwave absorption performance, Chem. Eng. J. 314 (2017) 477–487.

[69] M. Moser, C. Mondelli, A.P. Amrute, A. Tazawa, D. Teschner, M.E. Schuster, A. Klein-Hoffman, Nr. López, T. Schmidt, J. Pérez-Ramírez, HCl oxidation on IrO2-Based catalysts: from fundamentals to scale-up, ACS Catal. 3 (2013) 2813–2822.

[70] L. Atanasoska, R. Atanasoski, S. Trasatti, XPS and AES study of mixed layers of RuO2 and IrO2, Vacuum 40 (1990) 91–94.

[71] W. Sun, Z. Zhou, W.Q. Zaman, L.-m. Cao, J. Yang, Rational manipulation of IrO2 lattice strain on α-MnO2 nanorods as a highly efficient water-splitting catalyst, ACS Appl. Mater. Interfaces 9 (2017) 41855–41862.